Li, W., Liu, Z., Freddi, F. (2023). Non-smooth dynamic analysis of curved bridges considering the earthquake-induced end-pounding. Engineering Structures, 289: 116320. https://doi.org/10.1016/j.engstruct.2023.116320

Non-smooth dynamic analysis of curved bridges considering the earthquake-induced end-pounding

Wenshan Li[a], Zhao Liu[a,*], Fabio Freddi[b]
[a] School of Civil Engineering, Southeast University, Nanjing 210018, People's Republic of China
[b] Department of Civil, Environmental & Geomatic Engineering, University College London, London, UK
*Corresponding Author's e-mail address: mr.liuzhao@seu.edu.cn

Abstract
Curved beam bridges are widely used to accommodate the needs of complex transportation networks. However, these bridges are characterized by a complex dynamic response under earthquake excitation, and it is common to observe pounding-induced damages at the interfaces between adjacent beams or between the beam and the abutment after high-intensity earthquakes. The identification of pounding occurrences is a challenging task and highly dependent on the computational strategy used. The present paper addresses this problem by proposing and analyzing the suitability of an innovative non-smooth approach to solve the rigid bodies' dynamic response and contact interactions problem of curved beam bridges subjected to seismic ground motions. To this end, the dynamic equations of motions, including the pounding effects, are first formulated with the introduction of the Lagrange multipliers approach. The unilateral constraints are converted into a linear complementarity problem (LCP) formulation related to the velocity and impulse in the normal and transverse directions. The proposed algorithm of the differential equations in LCP form is successively implemented in Matlab to identify the collision and motion states by accessing the stepwise acceleration time history. A two-span curved beam bridge with an intermediate pier and two adjacent abutments under a single ground motion record is considered for case study purposes to investigate the suitability of the proposed procedure. The accuracy of the proposed method is verified by comparison with finite element (FE) analysis. The analysis results include the bridge's displacement time history and the motion states of all observed pounding occurrences. Finally, three validation methods, including the LCP relationship, the geometric relationship, and the momentum theorem, are evaluated to examine the validity of the proposed method. The results show that the proposed non-smooth dynamic formulation represents a new rigorous approach to identify and analyze the complex problem of end-pounding occurrence in curved bridges.

Keywords: Curved bridge; Seismic analysis; End-pounding; Non-smooth method; Linear complementarity problem approach.

1. Introduction

Curved beam bridges are widely used in the construction of highways and urban roads due to their ability to best fit complex road layouts and meet multiple traffic needs. However, due to their unique geometry, curved beam bridges are characterized by complex dynamic responses when subjected to earthquakes. It is a common scenario for curved beams to collide with adjacent beams or abutments (*i.e.,* seismic pounding) [1], producing severe seismic damage. Typical examples include the I-5/SR-14 interchange bridge during the San Fernando earthquake in 1971, the I-10/I-215 interchange bridge during the San Francisco earthquake in 1991 [2], the Southbound Separation Overpass during the Northridge earthquake in 1994 [3], and the Shiwei Bridge and Maoluoxi Bridge during the Taiwan Chi-Chi earthquake in 1999 [4]. More recently, during the 2008 Wenchuan earthquake in China, the curved portion of Baihua Bridge with a span arrangement of 5 × 20 m, shown in Fig. 1(a), experienced beam-unseating [1], while the southeast spiral concrete ramp of Huilan Interchange (Fig. 1(b)) suffered extensive damage [1].

(a) (b)

Fig. 1. Seismic damage of curved bridge during the 2008 Wenchuan earthquake: (a) Baihua Bridge; (b) Southeast ramp of Huilan interchange.

These damage scenarios highlight the significant need to advance knowledge in this field and to develop innovative, more effective, and efficient analysis tools to evaluate the seismic response of curved bridges under end-pounding effects. The identification of pounding occurrences is highly dependent on the computational strategy used. Among others, widely used methods rely on the use of force-based approaches [5] and include different arrangements of linear viscoelastic models [6,7], Hertz models [8], Hertz-damp models [9], and non-linear viscoelastic models [10,11]. These methods are the mainstream methods of collision analysis and are now widely used in the study of building [12-14] and bridge pounding [15-17]. These are phenomenological models, typically comprising spring elements, damping elements, and gap elements [18]. However, conventional force-based methods are characterized by some drawbacks. Among others, these methods are typically characterized by a time lag in the analysis, making them unsuitable for simulating instantaneous contact problems [19]. Such methods require velocities and positions to be continuous with time [20]. Additionally, the pounding forces are generated when the relative distance between two components tends to become negative, which obviously contradicts reality [21].

The beam-abutment system of a curved bridge under seismic load can be seen as a multi-body dynamic problem. When performing a seismic analysis of a multi-body system, it is important to find an accurate time value for the transition between the different states; specifically the transition between the non-contact and the contact states [22]. As the number of contacts increases, the detection process is very complex and becomes computationally demanding. Non-smooth approaches allow solving rigid bodies' dynamic response and contact interactions by converting unilateral constraints into a linear complementarity problem (LCP) [23-27]. LCP methods represent rigorous and effective ways to detect the actual contact events in non-smooth systems. In a multi-body system, the non-smooth method has advantages in terms of accuracy, reliability, and stability compared with the traditional force-based method. The present paper aims to investigate the seismic response of curved beam bridges, including the effects of seismic collisions, rather than the local damage caused by collisions. Additionally, these unilateral constraints prevent the penetration between the rigid bodies in contact by using an explicit formulation [28].

In the last few years, several research studies have used the non-smooth approach to assess the seismic response of bridge structures. Dimitrakopoulos [29,30] used the non-smooth approach to evaluate the complex dynamic response of earthquake-induced pounding between a beam and the abutment or between adjacent beams in skew bridges. Shi and Dimitrakopoulos [31] verified the effectiveness of the non-smooth approach while investigating the interaction between a beam and the abutment under an earthquake input and comparing the results with a shake-table test of a scaled deck-abutment bridge model. Shi and Dimitrakopoulos [32] assessed and compared the capacity of the non-smooth approach and force-based approaches to simulate the seismic response of a case study straight bridge. Additionally, Banerjee *et al.* [33] and Li *et al.* [34] calculated the complex dynamic behavior of pounding between a curved beam and an abutment or an adjacent beam. Banerjee *et al.* [35] simulated the pounding between a curved beam and an abutment and investigated the ideal combination of the column and bent arrangement and the gap distance.

According to the Author's knowledge, only the study from Banerjee *et al.* [33] used the non-smooth approach to study the collision problem of a curved beam bridge under earthquake loading. Moreover, this study did not analyze the two most important post-impact responses, namely the post-impact velocity and the impulses generated by impacts.

The present paper advances knowledge in this direction by developing a non-smooth approach for curved bridges which, not only evaluates the response after each impact event, but also analyzes the impact on the motion of the curved beam, and reveals the mechanism of the plane displacement and rotation of the curved beam caused by the collision. Three effective methods are proposed to evaluate the advantages and limitations of the proposed strategy for seismic impact dynamic analysis of curved beam bridges.

The paper is organized as follows. Firstly, an analytical model for curved beam bridges subjected to seismic excitation and subject to end-pounding is established. Next, the seismic response of a case study horizontal two-span curved beam bridge is investigated through the proposed method, and its accuracy is verified by comparison with finite element (FE) analysis. The pounding occurrences throughout the time history analysis are captured by the non-smooth approach, and the seismic motion is analyzed. Finally, the validity of the proposed method is examined by the LCP relationship, the geometric relationship, and the momentum theorem. The results confirm that the proposed method represents a new rigorous approach to identify and analyze the complex problem of end-pounding occurrence in curved bridges.

2. Non-smooth dynamic model for curved beam bridges

The proposed formulation to analyze the dynamic response of the curved bridge deck and pounding effects is based on the following assumptions:

1. The horizontal stiffness of the bridge deck is significantly greater than the lateral stiffness of its piers [19]. Hence, the curved beam, in the shape of an annular sector, can be modeled as a rigid body supported on piers and/or bearings when experiencing seismic excitations.
2. The mass of the piers is typically negligible with respect to the mass of the superstructure and does not significantly affect the seismic response. Hence, the dynamic equation of motion can be written by assuming the mass of the bridge deck as a lumped mass.
3. The sliding bearings on the abutments only provide vertical support to the curved beam without restraining the horizontal displacements.
4. The soil at the pier and abutments foundation is assumed stiff. Hence, soil-structure interaction effects are neglected in the present study.

2.1 Dynamic model

The planar dynamic model of a horizontally curved beam bridge is depicted in Fig. 2. The radius of the center line of the curved beam is denoted as R while the corresponding central angle is taken as β. The width of the curved beam is W, and the initial gap between the curved beam and the adjacent abutment is δ as shown in Fig. 2. The origin of the coordinate system is located at the center (O). The x-axis is horizontal to the right, and the y-axis is aligned with the symmetrical axis of the curved beam and points outward. The 3 degrees of freedom (DOF) of the model ($\boldsymbol{u}=[x_1, y_1, \theta_1]$) are assigned to the centroid (C_m). The connection point between the curved beam and the pier is denoted by the letter S. The four potential pounding spots of the curved beam ends adjacent to their abutments are indicated in red in Fig. 2. It should be noted that the considered case study bridge assumes a substructure with a single pillar pier with pier and beam consolidation. The problem formulation could be easily extended to other geometries by considering a different stiffness matrix for the system.

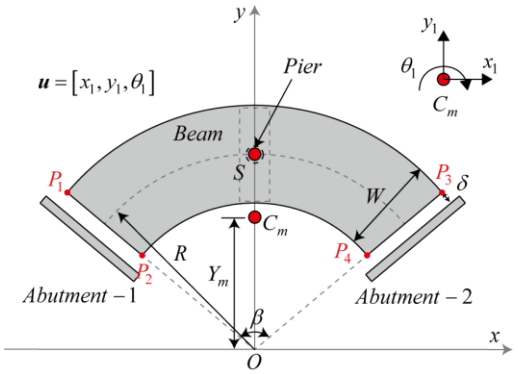

Fig. 2. Planar dynamic model of a horizontally curved beam bridge.

The mass (M) of the curved beam is given by:

$$M = A\rho R\beta \tag{1}$$

where A is the section area of the curved beam, and ρ is the uniform mass density of the curved beam. The y-axis coordinate (Y_m) of the centroid of the curved beam is calculated as follows:

$$Y_m = \frac{\int y dm}{M} = \frac{\iint_D y\rho dx dy}{M} = \left(2R + \frac{W^2}{6R}\right)\frac{\sin(\beta/2)}{\beta} \tag{2}$$

The geometric parameters of the box beam section are shown in Fig. 3. The moment of gyration (I_O) of the curved beam with respect to the original point in the xy coordinate system is calculated as follows:

$$I_O = \int r^2 dm = \frac{\rho\beta}{4}\cdot\left\{\sum_{i=1}^{2}[(R+\frac{W_i}{2})^4 - (R-\frac{W_i}{2})^4]\cdot h_i - [(R+\frac{W_3}{2})^4 - (R-\frac{W_3}{2})^4]\cdot h_3\right\} \tag{3}$$

where the definitions of W_i and h_i are displayed in Fig. 3.

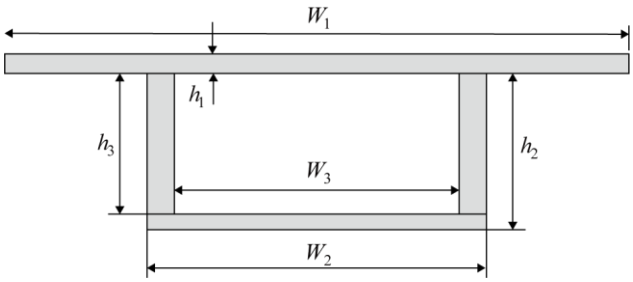

Fig. 3. Geometric parameters of the box beam section.

The parallel axis theorem is used to calculate the moment of gyration (I_M) of a curved beam with respect to the centroid of the curved beam in the xy coordinate system, as follows:

$$I_M = I_O - MY_m^2 \tag{4}$$

The mass matrix ($\boldsymbol{M}$) of this system is given as follows:

$$\boldsymbol{M} = diag\left(M, M, I_M\right) \tag{5}$$

The stiffness matrix ($\boldsymbol{K}_S$) of the bridge system with respect to the stiffness center *S* is given as follows:

$$\boldsymbol{K}_S = diag\left(\frac{3E\pi r_c^4}{h^3}, \frac{3E\pi r_c^4}{h^3}, \frac{G\pi r_c^4}{2h}\right) \tag{6}$$

where *E* and *G* represent the elastic and shear modulus of the concrete, respectively, while r_c and h denotes the radius and height of the pier. Eq. 6 is only valid for circular piers, but equivalent equations can be easily determined for other section shapes.

The stiffness matrix ($\boldsymbol{K}_M$) about the centroid of the curved beam is given as follows:

$$\boldsymbol{K}_M = \boldsymbol{T}^T \cdot \boldsymbol{K}_S \cdot \boldsymbol{T} \tag{7}$$

where the transformation matrix $\boldsymbol{T}$ is given as:

$$\boldsymbol{T} = \begin{bmatrix} 1 & 0 & Y_m - R \\ 0 & 1 & 0 \\ 0 & 0 & 1 \end{bmatrix} \tag{8}$$

2.2 Jacobian matrix

The initial geometric parameters of the curved beam are indicated in Fig. 4. The parameters r_{N1}, r_{N2}, r_{N3}, and r_{N4} represent the lever arms of the pertinent normal impulses with respect to the centroid of the curved beam. Similarly, r_{T1}, r_{T2}, r_{T3}, and r_{T4} are the lever arms of the relevant transverse impulses with respect to the centroid of the curved beam. The subscripts N and T are respectively used to represent the normal and transverse directions throughout the paper. The detailed formulation is provided by the following Eq.s (9).

$$
\begin{aligned}
r_{Ni} &= R + W/2 - Y_m \cdot \cos(\beta/2) \quad i = 1,3 \\
r_{Ni} &= R - W/2 - Y_m \cdot \cos(\beta/2) \quad i = 2,4 \\
r_{Ti} &= Y_m \cdot \sin(\beta/2) \quad i = 1,2,3,4
\end{aligned} \tag{9}
$$

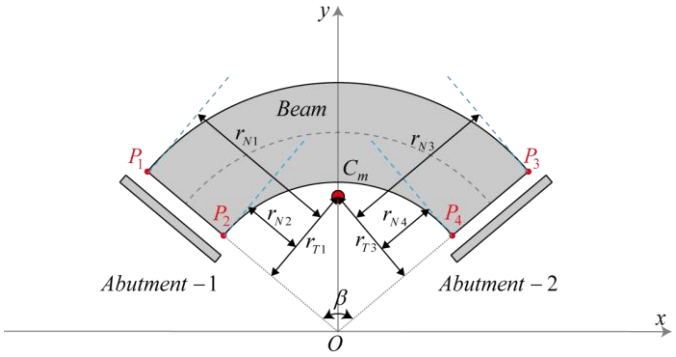

Fig. 4. Initial geometric parameters of the curved beam.

The geometric parameters of the curved beam in motion are displayed in Fig. 5. When the curved beam is in motion, $\tilde{r}_{N1}$, $\tilde{r}_{N2}$, $\tilde{r}_{N3}$, and $\tilde{r}_{N4}$ are the lever arms of the corresponding normal impulses, while $\tilde{r}_{T1}$, $\tilde{r}_{T2}$, $\tilde{r}_{T3}$, and $\tilde{r}_{T4}$ are the lever arms of the relevant transverse impulses. The detailed formulation is provided by the following Eq.s (10).

$$
\begin{aligned}
\tilde{r}_{Ni} &= r_{Ni} \cdot \cos\theta_1 + r_{Ti} \cdot \sin\theta_1 \quad i = 1,2 \\
\tilde{r}_{Ni} &= r_{Ni} \cdot \cos\theta_1 - r_{Ti} \cdot \sin\theta_1 \quad i = 3,4 \\
\tilde{r}_{Ti} &= -r_{Ni} \cdot \sin\theta_1 + r_{Ti} \cdot \cos\theta_1 \quad i = 1,2 \\
\tilde{r}_{Ti} &= r_{Ni} \cdot \sin\theta_1 + r_{Ti} \cdot \cos\theta_1 \quad i = 3,4
\end{aligned} \tag{10}
$$

The normal relative distances between the four potential pounding spots and the corresponding abutment are indicated in Fig. 5 and can be derived from the following Eq.s (11).

$$
\begin{aligned}
g_{Ni} &= \delta + x_1 \cdot \cos(\beta/2) + y_1 \cdot \sin(\beta/2) + r_{Ti} - \tilde{r}_{Ti} \quad i = 1,2 \\
g_{Ni} &= \delta - x_1 \cdot \cos(\beta/2) + y_1 \cdot \sin(\beta/2) + r_{Ti} - \tilde{r}_{Ti} \quad i = 3,4
\end{aligned} \tag{11}
$$

The normal relative velocities of the four spots are calculated by taking the derivative of Eq.s (11) with respect to time and are provided in the following Eq.s (12).

$$
\begin{aligned}
\dot{g}_{Ni} &= \dot{x}_1 \cdot \cos(\beta/2) + \dot{y}_1 \cdot \sin(\beta/2) + (r_{Ni} \cdot \cos\theta_1 + r_{Ti} \cdot \sin\theta_1)\dot{\theta}_1 \quad i = 1,2 \\
\dot{g}_{Ni} &= -\dot{x}_1 \cdot \cos(\beta/2) + \dot{y}_1 \cdot \sin(\beta/2) + (-r_{Ni} \cdot \cos\theta_1 + r_{Ti} \cdot \sin\theta_1)\dot{\theta}_1 \quad i = 3,4
\end{aligned} \tag{12}
$$

From $\dot{\boldsymbol{g}}_N = \boldsymbol{W}_N^T \dot{\boldsymbol{u}}$, the Jacobian matrix with normal constraints ($\boldsymbol{W}_N$) is derived as follows:

$$
\boldsymbol{W}_N = \begin{bmatrix}
\cos(\beta/2) & \cos(\beta/2) & -\cos(\beta/2) & -\cos(\beta/2) \\
\sin(\beta/2) & \cos(\beta/2) & \sin(\beta/2) & \sin(\beta/2) \\
\tilde{r}_{N1} & \tilde{r}_{N2} & -\tilde{r}_{N3} & -\tilde{r}_{N4}
\end{bmatrix} \tag{13}
$$

Similarly, the Jacobian matrix in the transverse direction ($\boldsymbol{W}_T$) is derived as follows:

$$\boldsymbol{W}_T = \begin{bmatrix} \sin(\beta/2) & \sin(\beta/2) & -\sin(\beta/2) & -\sin(\beta/2) \\ \cos(\beta/2) & \cos(\beta/2) & \cos(\beta/2) & \cos(\beta/2) \\ \tilde{r}_{T1} & \tilde{r}_{T2} & -\tilde{r}_{T3} & -\tilde{r}_{T4} \end{bmatrix} \tag{14}$$

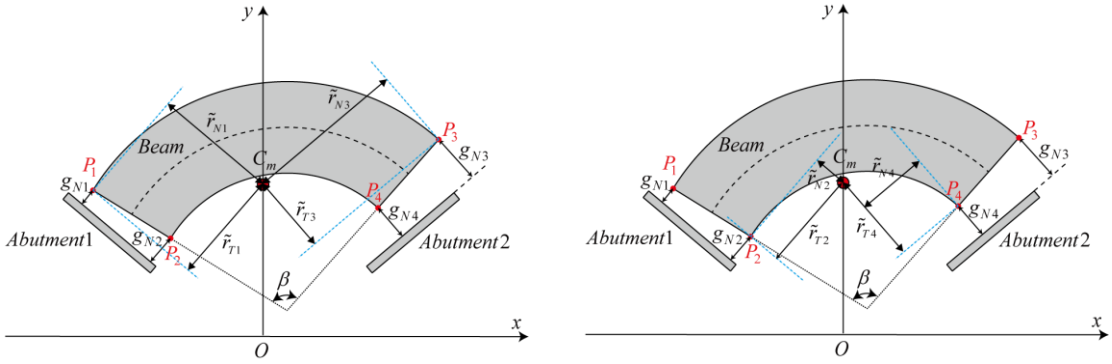

Fig. 5. Schematic representation of the geometric parameters of the curved beam in motion.(a) Parameters for spots 1 and 3; (b) Parameters for spots 2 and 4.

2.3 Non-smooth dynamic equations of motion for curved beam bridges

2.3.1 Linear complementarity Problem (LCP)

The system configuration considered is made of a curved beam with a single pillar and two abutments, which could result in multi-point contact when subjected to seismic actions. The proposed procedure aims at solving the multi-point contact problem by transforming the dynamic equation of motion into a LCP.

The LCP aims to identify two vectors that satisfy a specific inequality in a real vector space of limited dimensions [36]. Mathematically, a LCP aims at finding the two unknown non-negative complementary vectors $\boldsymbol{x}$ and $\boldsymbol{y}$ matching the following conditions:

$$\begin{aligned} \boldsymbol{y} &= \boldsymbol{A}\boldsymbol{x} + \boldsymbol{b} \\ \boldsymbol{x} \geq 0,\ \boldsymbol{y} &\geq 0,\ \boldsymbol{x}^{\mathrm{T}}\boldsymbol{y} = 0 \end{aligned} \tag{15}$$

where the matrices $\boldsymbol{A}$ and $\boldsymbol{b}$ are known (see Eq. (31) in the following section). It is claimed that the vectors $\boldsymbol{x}$ and $\boldsymbol{y}$ fulfill the LCP relationship.

In order to solve the collision problem between the beam and the abutments of a curved beam bridge under seismic excitation, the complementarity form of Newton's impact law in the normal direction is established in Section 2.3.2. Similarly, the complementary form of Coulomb's friction law in the transverse direction is established in Section 2.3.3. Based on the contents of Sections 2.3.2 and 2.3.3, the LCP form of the system dynamics equation under seismic excitation is established in Section 2.3.4.

2.3.2 The complementarity form of Newton's impact law in the normal direction

The Newton's impact law [37] is used to describe the impact process in the normal direction. The post-impact velocity ($\dot{g}_{Ni}^{+}$) of contact point '*i*' (see Fig. 5) is given as follows:

$$\dot{g}_{Ni}^{+} = -\varepsilon_{Ni}\dot{g}_{Ni}^{-} \tag{16}$$

where $\dot{g}_{Ni}^{-}$ is the pre-impact velocity and ε_{Ni} represents the coefficient of restitution in the normal direction, which varies between zero and one (*i.e.*, $\varepsilon_{Ni} \in [0,1]$). For a multi-point contact problem, ε_{Ni} can be written as a matrix $\boldsymbol{\varepsilon}_{Ni} = diag\{\varepsilon_{Ni}\}$, and Eq. (16) can take the following matrix form:

$$\dot{\boldsymbol{g}}_N^+ = -\boldsymbol{\varepsilon}_N \dot{\boldsymbol{g}}_N^- \tag{17}$$

The vector $\boldsymbol{\xi}_N$, referred to as the normal synthetic velocity hereinafter, represents the linear combination of post-impact velocity $\dot{g}_{Ni}^+$ and pre-impact velocity $\dot{g}_{Ni}^-$ and can be defined as follows:

$$\boldsymbol{\xi}_N = \dot{\boldsymbol{g}}_N^+ + \boldsymbol{\varepsilon}_N \dot{\boldsymbol{g}}_N^- \tag{18}$$

When the curved beam and abutment come into contact, the normal impulse vector of the contact points $\boldsymbol{\Lambda}_N \geq 0$ while the normal synthetic velocity vector $\boldsymbol{\xi}_N = 0$. Conversely, when there is no contact, $\boldsymbol{\Lambda}_N = 0$ and $\boldsymbol{\xi}_N \geq 0$. $\boldsymbol{\Lambda}_N$ is the normal impulse vectors due to the impact with $\boldsymbol{\Lambda}_N = diag(\Lambda_{Ni})$ where Λ_{Ni} represents the normal impulse of contact point *'i'* (see Fig. 5).

Therefore, the LCP formulation can be established from the Newton's impact law as follows:

$$\boldsymbol{\Lambda}_N \geq 0, \quad \boldsymbol{\xi}_N \geq 0, \quad \boldsymbol{\Lambda}_N^T \boldsymbol{\xi}_N = 0 \tag{19}$$

2.3.3 The complementarity form of Coulomb's friction law in the transverse direction

The Coulomb's friction law is used to describe the conditions for transverse constraints. With regard to friction, the following three conditions are possible:

$$\begin{aligned} \dot{g}_{Ti} = 0 \quad &\Rightarrow \quad |\Lambda_{Ti}| \leq \mu_i \Lambda_{Ni} \quad (\text{sticking}) \\ \dot{g}_{Ti} < 0 \quad &\Rightarrow \quad |\Lambda_{Ti}| = +\mu_i \Lambda_{Ni} \quad (\text{negative sliding}) \\ \dot{g}_{Ti} > 0 \quad &\Rightarrow \quad |\Lambda_{Ti}| = -\mu_i \Lambda_{Ni} \quad (\text{positive sliding}) \end{aligned} \tag{20}$$

where μ_i represents the Coulomb's friction coefficient of contact point '*i*' (see Fig. 5), $\dot{g}_{Ti}$ represents the relative velocity of contact point '*i*', while Λ_{Ni} and Λ_{Ti} represent the normal and transverse impulse of contact point '*i*', respectively. Fig. 6 shows the three friction conditions of Eq. (20).

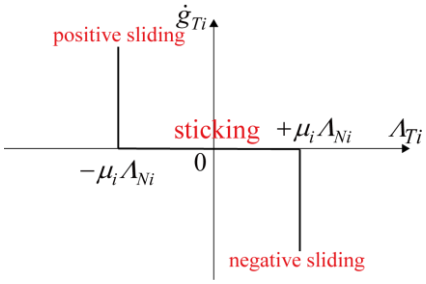

Figure 6. Conditions for transverse constraints according to Coulomb's friction law.

The relative transverse velocity and transverse impulse can be split into two parts and decomposed as in the following Eq.s (21) and (22) and as shown in Figs. 7(b) and (c).

$$\begin{aligned} \dot{g}_{Ti} &= \xi_{Ri} - \xi_{Li} \\ \xi_{Ri} &= \left(|\dot{g}_{Ti}| + \dot{g}_{Ti}\right)/2 \geq 0 \\ \xi_{Li} &= \left(|\dot{g}_{Ti}| - \dot{g}_{Ti}\right)/2 \geq 0 \end{aligned} \tag{21}$$

$$\begin{aligned} \Lambda_{Ti} &= \left(\Lambda_{Ri} - \Lambda_{Li}\right)/2 \\ \Lambda_{Ri} &= \mu_i \Lambda_{Ni} + \Lambda_{Ti} \\ \Lambda_{Li} &= \mu_i \Lambda_{Ni} - \Lambda_{Ti} \end{aligned} \tag{22}$$

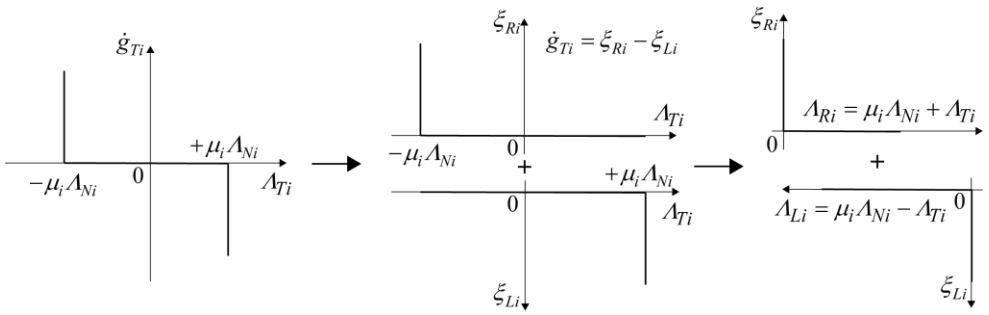

Figure 7. Decomposition of the friction characteristic. (a) Coulomb's friction law; (b) Decomposition of the relative transverse velocities; (c) Decomposition of the transverse impulses.

From Fig. 7(c), the LCP formulation can be established as follows:

$$\begin{aligned} &\Lambda_{Ri} \geq 0, \qquad \boldsymbol{\xi}_{Ri} \geq 0, \qquad \Lambda_{Ri}^T \boldsymbol{\xi}_{Ri} = 0, \\ &\Lambda_{Li} \geq 0, \qquad \boldsymbol{\xi}_{Li} \geq 0, \qquad \Lambda_{Li}^T \boldsymbol{\xi}_{Li} = 0. \end{aligned} \tag{23}$$

Moreover, Eq. (23) can take the following matrix form:

$$\begin{aligned} &\boldsymbol{\Lambda}_R \geq 0, \qquad \boldsymbol{\xi}_R \geq 0, \qquad \boldsymbol{\Lambda}_R^T \boldsymbol{\xi}_R = 0, \\ &\boldsymbol{\Lambda}_L \geq 0, \qquad \boldsymbol{\xi}_L \geq 0, \qquad \boldsymbol{\Lambda}_L^T \boldsymbol{\xi}_L = 0, \end{aligned} \tag{24}$$

where $\boldsymbol{\mu} = diag(\mu_i)$, $\boldsymbol{\Lambda}_R = diag(\Lambda_{Ri})$, $\boldsymbol{\Lambda}_L = diag(\Lambda_{Li})$, $\boldsymbol{\xi}_R = diag(\boldsymbol{\xi}_{Ri})$ and $\boldsymbol{\xi}_L = diag(\boldsymbol{\xi}_{Li})$.

2.3.4 Non-smooth dynamic equation of motion

The dynamic equation of a multi-DOFs system under seismic excitation can be written as follows:

$$\boldsymbol{M}\ddot{\boldsymbol{u}} + \boldsymbol{C}\dot{\boldsymbol{u}} + \boldsymbol{K}\boldsymbol{u} = -\boldsymbol{M}\ddot{\boldsymbol{u}}_g \tag{25}$$

where $\boldsymbol{M}$, $\boldsymbol{C}$, and $\boldsymbol{K}$ are, respectively, the mass matrix, damping matrix, and stiffness matrix of the curved bridge system. The generalized acceleration vector, generalized velocity vector, and generalized displacement vector are designated as $\ddot{\boldsymbol{u}}$, $\dot{\boldsymbol{u}}$, and $\boldsymbol{u}$, respectively. The seismic acceleration vector is represented by $\ddot{\boldsymbol{u}}_g$.

The solution of Eq. (25) is based on the solution of a set of simultaneous differential equations as follows:

$$\dot{\boldsymbol{X}}(t) = \begin{bmatrix} \boldsymbol{0} & \boldsymbol{I} \\ -\boldsymbol{M}^{-1}\boldsymbol{K} & -\boldsymbol{M}^{-1}\boldsymbol{C} \end{bmatrix} \boldsymbol{X}(t) + \begin{bmatrix} \boldsymbol{0} \\ -\ddot{\boldsymbol{u}}_g \end{bmatrix} \tag{26}$$

where $\boldsymbol{X}(t) = \begin{bmatrix} \boldsymbol{u}(t) & \dot{\boldsymbol{u}}(t) \end{bmatrix}^T$, which denotes the vector of displacement and velocity, which has the zero initial condition $\boldsymbol{X}(0) = \begin{bmatrix} \boldsymbol{0} & \boldsymbol{0} \end{bmatrix}^T$.

When the curved beam impacts the adjacent abutment due to high-intensity ground motions, the contact with the abutments changes the boundary conditions of the problem. By introducing the impact and friction force to the fundamental dynamic equation (Eq. (25)) and using the Lagrange multiplier approach to create the dynamic equation of motion for the non-smooth pounding system, it yields:

$$\boldsymbol{M}\ddot{\boldsymbol{u}} + \boldsymbol{C}\dot{\boldsymbol{u}} + \boldsymbol{K}\boldsymbol{u} - \boldsymbol{W}_N\boldsymbol{\lambda}_N - \boldsymbol{W}_T\boldsymbol{\lambda}_T = -\boldsymbol{M}\ddot{\boldsymbol{u}}_g \tag{27}$$

where $\boldsymbol{\lambda}_N$ and $\boldsymbol{\lambda}_T$ represent the impact and friction force vectors in normal and transverse directions,

respectively.

Assuming that the pounding process begins at t^- and ends at t^+, and considering that according to the rigid body dynamics problem, the time difference $\Delta t = t^+ - t^-$ can be considered infinitesimal, the dynamic Eq. (27) on Δt can be integrated to obtain the following equation:

$$\begin{aligned} &\boldsymbol{M}\left(\dot{\boldsymbol{u}}^+ - \dot{\boldsymbol{u}}^-\right) - \boldsymbol{W}_N \boldsymbol{\Lambda}_N - \boldsymbol{W}_T \boldsymbol{\Lambda}_T = -\left(\boldsymbol{M}\ddot{\boldsymbol{u}}_g + \boldsymbol{C}\dot{\boldsymbol{u}} + \boldsymbol{K}\boldsymbol{u}\right)\Delta t = \boldsymbol{0}, \\ &\boldsymbol{\Lambda}_N = \lim_{t^+ \to t^-} \int_{t^-}^{t^+} \boldsymbol{\lambda}_N dt, \boldsymbol{\Lambda}_T = \lim_{t^+ \to t^-} \int_{t^-}^{t^+} \boldsymbol{\lambda}_T dt. \end{aligned} \tag{28}$$

where $\dot{\boldsymbol{u}}^-$ and $\dot{\boldsymbol{u}}^+$ represent the generalized velocity vectors before and after pounding, respectively. The superscripts "-" and "+" denote the pre- and post-impact states, respectively.

However, the solution of Eq.s (28) is an indeterminate problem (*i.e.,* two equations and three unknown vectors). The LCP approach helps address the problem by defining a set of equations that relates velocity and force.

In the contact kinematics of rigid bodies, with the help of the Jacobian matrix, the relative velocities between objects can be expressed as a linear combination of generalized velocities, namely:

$$\begin{aligned} \dot{g}_N\left(\boldsymbol{u},t\right) &= \frac{\partial g_N}{\partial \boldsymbol{u}}\dot{\boldsymbol{u}} + \frac{\partial g_N}{\partial t} = \boldsymbol{W}_N^T \dot{\boldsymbol{u}} + \tilde{w}_N \\ \dot{g}_T\left(\boldsymbol{u},t\right) &= \frac{\partial g_T}{\partial \boldsymbol{u}}\dot{\boldsymbol{u}} + \frac{\partial g_T}{\partial t} = \boldsymbol{W}_T^T \dot{\boldsymbol{u}} + \tilde{w}_T \end{aligned} \tag{29}$$

Hence, the relative velocities between objects before and after impact are:

$$\begin{aligned} \dot{g}_N^- &= \boldsymbol{W}_N^T \dot{\boldsymbol{u}}^- + \tilde{w}_N \quad , \quad \dot{g}_T^- = \boldsymbol{W}_T^T \dot{\boldsymbol{u}}^- + \tilde{w}_T, \\ \dot{g}_N^+ &= \boldsymbol{W}_N^T \dot{\boldsymbol{u}}^+ + \tilde{w}_N \quad , \quad \dot{g}_T^+ = \boldsymbol{W}_T^T \dot{\boldsymbol{u}}^+ + \tilde{w}_T. \end{aligned} \tag{30}$$

From Eq. (19), (24), (28), and (30), the dynamic equation of motion of a curved beam bridge considering seismic excitation and end-pounding is transformed into a LCP form, leading to a set of closed-form equations as follows:

$$\underbrace{\begin{bmatrix} \boldsymbol{\xi}_N \\ \boldsymbol{\xi}_R \\ \boldsymbol{\Lambda}_L \end{bmatrix}}_{\boldsymbol{y}} = \underbrace{\begin{bmatrix} \boldsymbol{W}_N^T \boldsymbol{M}^{-1}\left(\boldsymbol{W}_N - \boldsymbol{\mu}\cdot\boldsymbol{W}_T\right) & \boldsymbol{W}_N^T \boldsymbol{M}^{-1}\boldsymbol{W}_T & \boldsymbol{0} \\ \boldsymbol{W}_T^T \boldsymbol{M}^{-1}\left(\boldsymbol{W}_N - \boldsymbol{\mu}\cdot\boldsymbol{W}_T\right) & \boldsymbol{W}_T^T \boldsymbol{M}^{-1}\boldsymbol{W}_T & \boldsymbol{I} \\ 2\boldsymbol{\mu} & -\boldsymbol{I} & \boldsymbol{0} \end{bmatrix}}_{\boldsymbol{A}} \cdot \underbrace{\begin{bmatrix} \boldsymbol{\Lambda}_N \\ \boldsymbol{\Lambda}_R \\ \boldsymbol{\xi}_L \end{bmatrix}}_{\boldsymbol{x}} + \underbrace{\begin{bmatrix} \left(\boldsymbol{\varepsilon}_N + \boldsymbol{I}\right)\dot{\boldsymbol{u}}_N^- \\ \dot{\boldsymbol{g}}_T^- \\ \boldsymbol{0} \end{bmatrix}}_{\boldsymbol{b}} \tag{31}$$

Eq. (26) can be solved directly using the direct integration approach (Runge-Kutta method) implemented in Matlab, while Lemke's pivotal algorithm [36] is used to solve Eq. (31).

3. Numerical example

3.1 Case study circular curved bridge

Fig. 6 shows the horizontally curved bridge comprising two spans, an intermediate pier, and two adjacent abutments, considered for case study purposes. The superstructure is a box girder with a 31 m span length and 8 m width. The circular beam has a central radius R of 60 m and subtended angle β equal to 60°. The pier has a height of 10 m with a diameter of 1.2 m. The curved beam and the pier are monolithically cast, and the elastomeric bearings with PTFE topping are positioned on both sides of the abutment. The friction coefficient for PTFE is typically low and assumed negligible. The gap between the curved beam end and the adjacent abutments is equal to 0.06 m. The curved bridge is designed according to 'Specifications for Seismic Design of Highway

Bridges' in China (hereafter referred to as Chinese code) [38] considering a seismic fortification intensity of 7 with a peak ground acceleration (PGA) equal to 0.10g according to Chinese specification. The normal impact coefficient is assumed as 0.5, while the Coulomb friction coefficient is assumed as 0.3. The stiffness center of the system coincides with the position of the pier, denoted by the letter S, while the centroid of the curved beam is indicated as C_m.

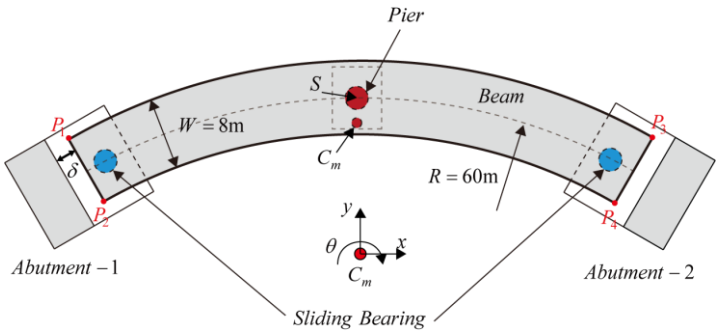

Fig. 6. Plan view of the case study bridge.

A box section similar to the one illustrated in Fig. 3 is assumed, with the following geometric parameters: W_1 = 8 m; W_2 = 4.35 m; W_3 = 3.65 m; h_1 = 0.25 m; h_2 = 1.775 m; and h_3 = 1.975 m. The cross-section area (A) equals 4.11 m^2.

The mass matrix of the dynamic system is determined by Eq. (5).

$$\boldsymbol{M} = diag\left(0.672, 0.672, 256.2\right)\times 10^6 \quad \text{kNsec}^2/\text{m} \tag{32}$$

The stiffness matrix with respect to the centroid is obtained by Eq. (7).

$$\boldsymbol{K}_M = \begin{bmatrix} 4.28 & 0 & -11.2 \\ 0 & 4.28 & 0 \\ -11.2 & 0 & 60.0 \end{bmatrix} \times 10^7 \quad \text{kN/m} \tag{33}$$

3.2 Selected ground motion

The ground motion records in x- and y-direction (see Fig. 6) of the 1999 Chi-Chi earthquake in Taiwan are selected to investigate and compare the proposed strategy with alternative analysis options. The records' PGA is scaled to 0.4g in both directions. The two components of the chosen ground motion are shown in Fig. 7, together with their respective acceleration, velocity, and displacement time histories. These records have a duration of approximately 30 sec and a time step size of 0.005 s.

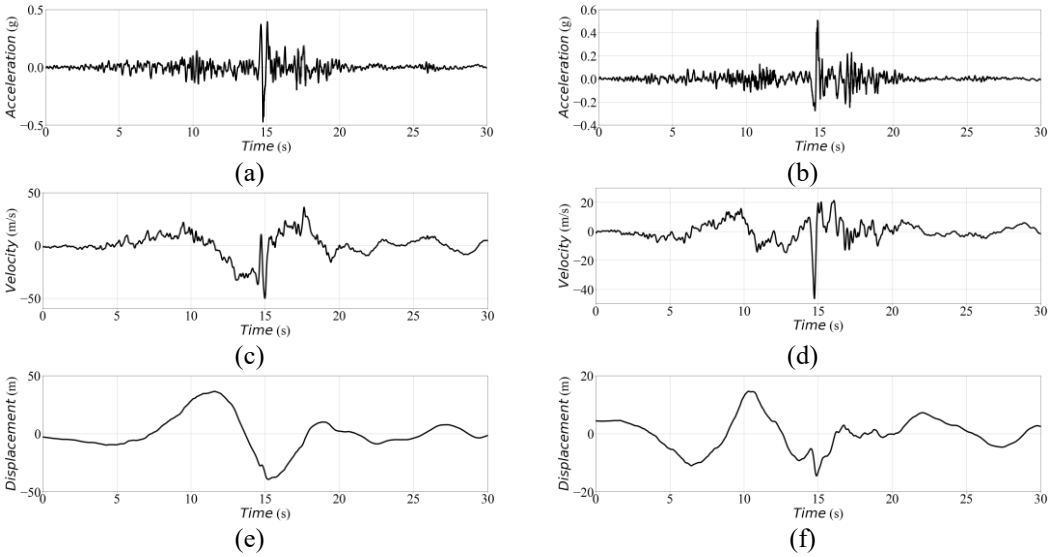

Fig. 7. 1999 Chi-Chi earthquake in Taiwan. Unscaled acceleration, velocity, and displacement time histories in (a) x-direction; and (b) y-direction.

3.3 Finite element (FE) modeling of the case study curved bridge

A simplified elastic 3D FE model of the case study circular curved bridge is developed in OpenSees [39] and successively used to validate the proposed model. Fig. 8(a) and (b) show, respectively, the *x*-*y* and the *x*-*z* views of the FE model. The beam and pier are modeled as 'elasticBeamColumn' elements in OpenSees with the parameters summarized in Table 1. The curved beam is consolidated with the middle pier and restricted to move only in the plane, while the pier is fixed at the base. Eight straight segments have been included in the model to represent the curved beam. A parametric analysis showed that a finer discretization does not significantly affect the results. The masses and the gravity loads have been uniformly distributed among the nodes of the curved beam. The values of the mass-related and stiffness-related Rayleigh damping coefficients are evaluated for a damping factor of 5%, considering the first and the second vibration modes. The material and geometric non-linearities and the soil-structure interaction are neglected in this model.

Table 1. Parameters of the 'elasticBeamColumn' elements in OpenSees.

Components	A (m^2)	E (MPa)	G (MPa)	J (m^4)	I_y (m^4)	I_z (m^4)
Beam	4.11	3.5×10^{-4}	1.51×10^{-4}	12.69	8.87	20.63
Pier	1.13	3.5×10^{-4}	1.51×10^{-4}	2.04×10^{-1}	1.02×10^{-1}	1.02×10^{-1}

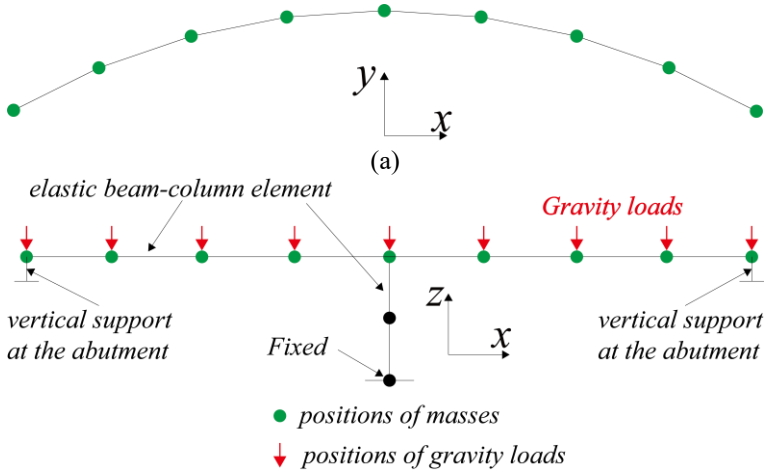

Fig. 8. 3D elastic finite element (FE) model of the case study circular curved bridge. (a) *x*-*y* view; (b) *x*-*z* view.

3.4 Preliminary seismic response analysis ignoring the pounding effects

The seismic response of the curved bridge is initially simulated by ignoring the pounding effects. Specifically, the proposed model is compared with the FE model presented in Section 3.3.

Fig. 9 shows the response history in terms of lateral displacements of point *S*, *i.e.,* connection point between the curved beam and the pier. The comparison shows a very good agreement of the results both in *x*- and *y*-direction. A slight difference between the two simulations is observed in a few transitory peaks. Fig. 9(a) shows the displacement time history in the *x*-direction for which the peak displacement is attained at 15.790 s. In this instant, the results of the proposed and OpenSees models are 0.0467 m and 0.0462 m, respectively (*i.e.,* error of approximately 1%). Fig. 9(b) shows the displacement time history in the *y*-direction. In this case, the peak displacement is observed at 16.325 s with displacement values from the proposed and OpenSees models are 0.0776 m and 0.0799 m, respectively (*i.e.,* error of approximately 3%). These preliminary results show that, in the absence of pounding effects, the proposed model satisfactorily captures the seismic response of the curved bridge.

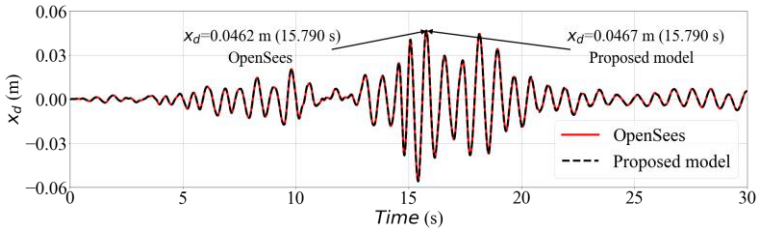

(a)

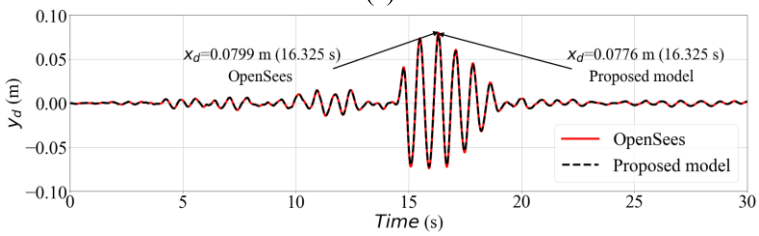

(b)

Fig. 9. Comparison of the displacement time history of point *S* neglecting the earthquake-induced end-pounding. Proposed model *vs.* OpenSees model in the (a) *x*-; and (b) *y*-direction.

3.5 Seismic response analysis considering the pounding effects

The seismic response of the case study curved bridge is successively simulated, accounting for earthquake-induced end-pounding through the proposed model. Fig. 10 shows the seismic displacement response of point C_m in the *x*- and *y*-direction. All pounding occurrences and their corresponding pounding states are labeled. Specifically, six pounding occurrences have occurred during the whole time history at time 15.045 s, 15.240 s, 15.885 s, 16.445 s, 17.290 s, and 18.145 s. These include 2 collisions at points P_1 and P_3, 1 collision at point P_4, and 1 simultaneous collision at points P_1 and P_2. Similarly, Fig. 11 shows the time histories of the normal forces λ_{Ni}, the normal relative distances g_{Ni}, and the pounding occurrences marked by red circles. Fig. 12 shows the displacement configuration of the curved bridge for all pounding occurrences.

Fig. 12(a) shows the pounding occurrence at 15.045 s where a contact is observed at spot P_4. The centroid of the curved beam moves 35.8 mm and -62.5 mm in the *x*- and *y*-directions, respectively, and the counterclockwise rotation is $-3.39\cdot10^{-4}$ rad. This displacement induces the curved beam to collide with the right abutment at P_4. g_{N1}, g_{N2}, g_{N3}, and g_{N4} are, respectively, 55 mm, 58 mm, 3mm, and 0. At this moment, the normal pounding force λ_{N4} and the transverse friction force λ_{T4} at P_4 are 91443 kN and -25985 kN, respectively. The resultant force of λ_{N4} and λ_{T4}, λ_{R4}, causes the velocity of the centroid of the curved beam drops from 237.4 mm/s to -255.3 mm/s in the *x*-direction and rises from -266.2 mm/s to -93.4 mm/s in the *y*-direction. The angular velocity at the centroid of the curved beam increases from $-1.64\cdot10^{-3}$ rad/s to $1.63\cdot10^{-3}$ rad/s as a consequence of the clockwise moment produced by λ_{N4} and λ_{T4}. The moment is equal to 91443× $\tilde{r}_{N4}$ -25985× $\tilde{r}_{T4}$ =173062 kNm.

Fig. 12(b) shows the pounding occurrence at 15.240 s where simultaneous contacts are observed at spots P_1 and P_2. The centroid of the curved beam moves -59.9 mm and -17.2 mm in the *x*- and *y*-directions, respectively, and rotates $1.03\cdot10^{-5}$ rad clockwise. This displacement induces the curved beam to collide with the left abutment at P_1 and P_2. g_{N1}, g_{N2}, g_{N3}, and g_{N4} are, respectively, 0, 0, 103 mm, and 103 mm. At this moment, the normal pounding force λ_{N1} and the transverse friction force λ_{T1} at P_1 are 35291 kN and -10587 kN, respectively. The normal pounding force λ_{N2} and the transverse friction force λ_{T2} at P_2 are 33332 kN and -10000 kN, respectively. The resultant force λ_R, causes the velocity of the centroid of the curved beam rises from -428.3 mm/s to -213.1 mm/s in the *x*-direction and rises from 445.2 mm/s to 517.4 mm/s in the *y* direction. The angular velocity at the centroid of the curved beam drops from $-4.74\cdot10^{-4}$ rad/s to $-2.37\cdot10^{-4}$ rad/s as a consequence of the counterclockwise moment produced by λ_R. The moment is equal to 35291× $\tilde{r}_{N1}$ -10587× $\tilde{r}_{T1}$ +33332× $\tilde{r}_{N2}$ -10000× $\tilde{r}_{T2}$ =-76805 kNm.

Fig. 12(c) shows the pounding occurrence at 15.885 s where a contact is observed at spot P_1. The centroid of the curved beam moves -9.3 mm and -70.6 mm in the x- and y-directions, respectively, and rotates $-1.23\cdot10^{-3}$ rad counterclockwise. The displacements induce the curved beam to collide with the left abutment at P_1. g_{N1}, g_{N2}, g_{N3}, and g_{N4} are, respectively, 0, 9 mm, 50 mm, and 41 mm. At this moment, the normal pounding force λ_{N1} and the transverse friction force λ_{T1} at P_1 are 84820 kN and -25446 kN, respectively. The resultant force of λ_{N1} and λ_{T1}, λ_{R1}, causes the velocity of the centroid of the curved beam rises from -517.1 mm/s to -65.1 mm/s in the x-direction and rises from 28.0 mm/s to 179.6 mm/s in the y-direction. The angular velocity at the centroid of the curved beam increases from $-2.33\cdot10^{-3}$ rad/s to $1.17\cdot10^{-2}$ rad/s as a consequence of the clockwise moment produced by λ_{N1} and λ_{T1}. The moment is equal to 84820× $\tilde{r}_{N1}$ -25446× $\tilde{r}_{T1}$ =516410 kNm.

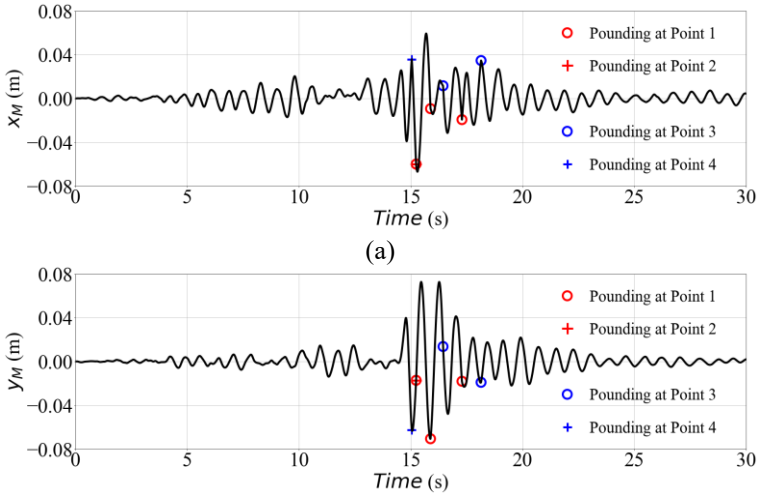

Fig. 10. Displacement time history of point C_m of the curved beam considering earthquake-induced end-pounding in the (a) x-; and (b) y-direction.

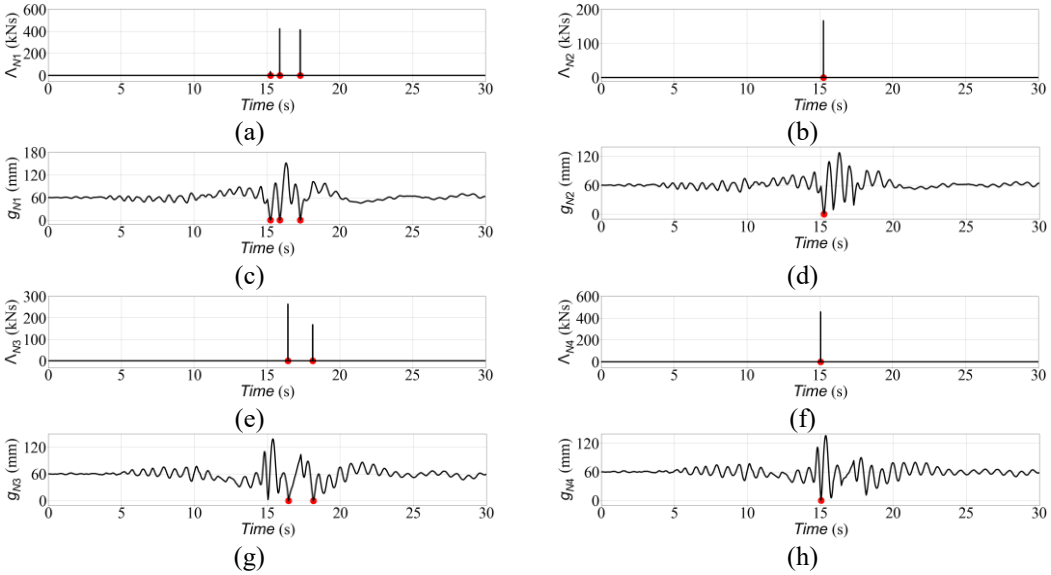

Fig. 11. Time histories of the normal impulse forces and relative distance between each impact spot and abutments: (a) Λ_{N1}; (b) Λ_{N2}; (c) g_{N1}; (d) g_{N2}; (e) Λ_{N3}; (f) Λ_{N4}; (g) g_{N3}; (h) g_{N4}.

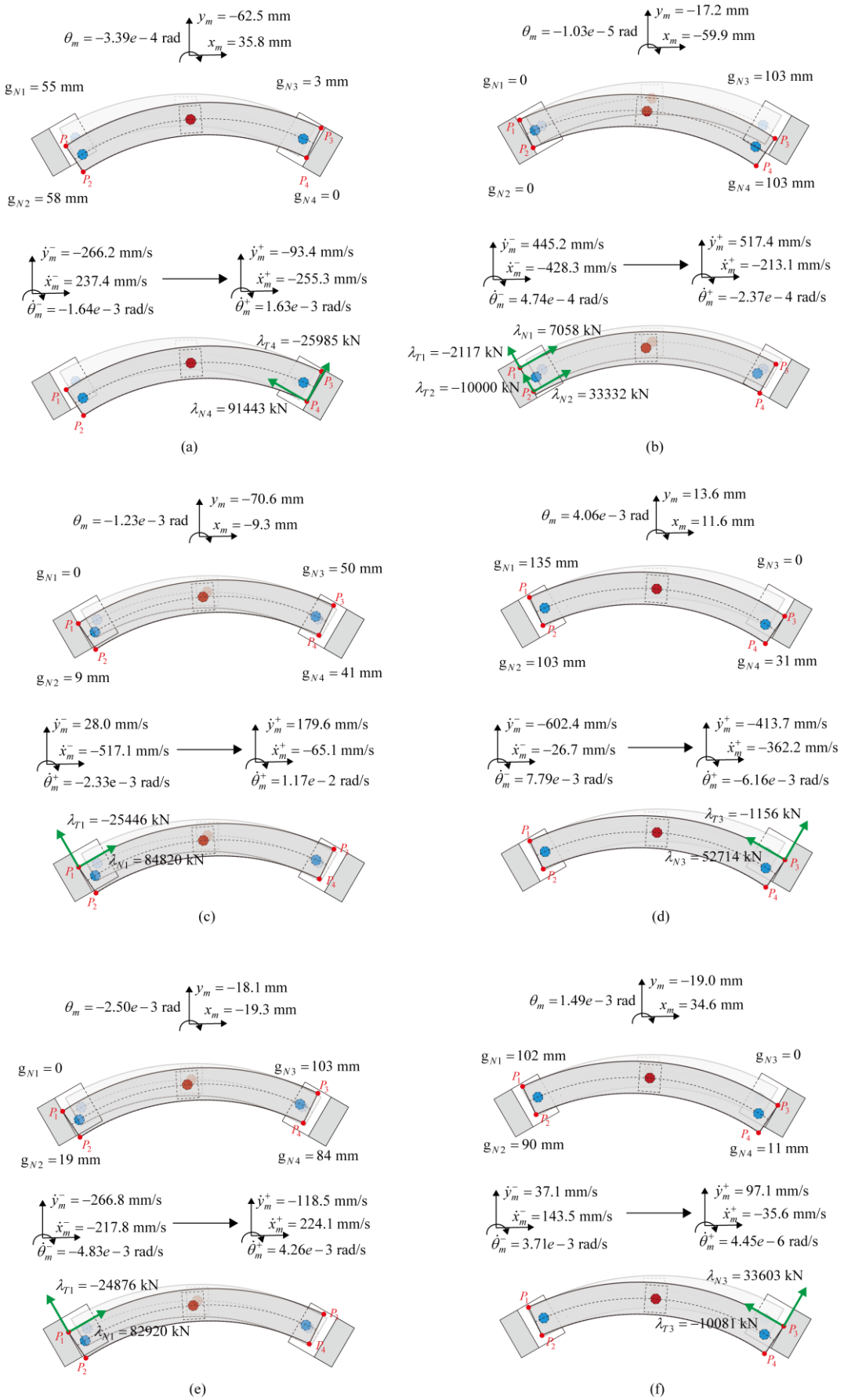

Fig. 12. Displacement configuration of the curved bridge at (a) 15.045 s; (b) 15.240 s; (c) 15.885 s; (d) 16.445 s; (e) 17.290 s; (f) 18.145 s.

Fig. 12(d) shows the pounding occurrence at 16.445 s where a contact is observed at spot P_3. The centroid of the curved beam moves 11.6 mm and 13.6 mm in the *x*- and *y*-directions, respectively, and rotates $4.06 \cdot 10^{-3}$ rad clockwise. This displacement induces the curved beam to collide with the right abutment at P_3. g_{N1}, g_{N2}, g_{N3}, and g_{N4} are, respectively, 135 mm, 103 mm, 0, and 31 mm. At this moment, the normal pounding force λ_{N3} and the transverse friction force λ_{T3} at P_3 are 52714 kN and -1156 kN, respectively. The resultant force of λ_{N3} and λ_{T3}, λ_{R3}, causes the velocity of the centroid of the curved beam drops from -26.7 mm/s to -362.2 mm/s in the *x*-direction and rises from -602.4 mm/s to -413.7 mm/s in the *y* direction. The angular velocity at the centroid of the curved beam drops from $7.79 \cdot 10^{-3}$ rad/s to - $6.16 \cdot 10^{-3}$ rad/s as a consequence of the counterclockwise moment produced by λ_{N3} and λ_{T3}. The moment is equal to 52714× $\tilde{r}_{N3}$ -1156× $\tilde{r}_{T3}$=-730520 kNm.

Fig. 12(e) shows the pounding occurrence at 17.290 s where a contact is observed at spot P_1. The centroid of the curved beam moves -19.3 mm and -18.1 mm in the *x*- and *y*-directions, respectively, and rotates - $2.50 \cdot 10^{-3}$ rad counterclockwise. The displacements induce the curved beam to collide with the left abutment at P_1. g_{N1}, g_{N2}, g_{N3}, and g_{N4} are, respectively, 0, 19 mm, 103 mm, and 84 mm. At this moment, the normal pounding force λ_{N1} and the transverse friction force λ_{T1} at P_1 are 82920 kN and -24876 kN, respectively. The resultant force of λ_{N1} and λ_{T1}, λ_{R1}, causes the velocity of the centroid of the curved beam rises from -217.8 mm/s to 224.1 mm/s in the *x*-direction and rises from -266.8 mm/s to -118.5 mm/s in the *y*-direction. The angular velocity at the centroid of the curved beam increases from - $4.84 \cdot 10^{-3}$ rad/s to $4.26 \cdot 10^{-3}$ rad/s as a consequence of the clockwise moment produced by λ_{N1} and λ_{T1}. The moment is equal to 82920× $\tilde{r}_{N1}$ -24876× $\tilde{r}_{T1}$ =484532 kNm.

Fig. 12(f) shows the pounding occurrence at 18.145 s where a contact is observed at spot P_3. The centroid of the curved beam moves 34.6 mm and -19.0 mm in the *x*- and *y*-directions, respectively, and rotates $1.49 \cdot 10^{-3}$ rad clockwise. This displacement induces the curved beam to collide with the right abutment at P_3. g_{N1}, g_{N2}, g_{N3}, and g_{N4} are, respectively, 102 mm, 90 mm, 0, and 11 mm. At this moment, the normal pounding force λ_{N3} and the transverse friction force λ_{T3} at P_3 are 33603 kN and -10081 kN, respectively. The resultant force of λ_{N3} and λ_{T3}, λ_{R3}, causes the velocity of the centroid of the curved beam drops from 143.5 mm/s to -35.6 mm/s in the *x*-direction and rises from 37.1 mm/s to 97.1 mm/s in the *y* direction. The angular velocity at the centroid of the curved beam drops from $3.71 \cdot 10^{-3}$ rad/s to $4.45 \cdot 10^{-6}$ rad/s as a consequence of the counterclockwise moment produced by λ_{N3} and λ_{T3}. The moment is equal to 33603× $\tilde{r}_{N3}$ -10081× $\tilde{r}_{T3}$=-191634 kNm.

These results are summarized in Table 2 which lists the key parameters of the solution for the six pounding occurrences, including *1)* the occurring time, *2)* the pounding spots (P_i) with the abutments, *3)* the normal and transverse input forces (λ_{Ni} , and λ_{Ti}), *4)* the displacements (x_m , y_m , and θ_m) of the centroid of the curved beam, *5)* the normal relative distances (g_{Ni}), *6)* the pre-impact velocities ($\dot{x}_m^-$, $\dot{y}_m^-$, and $\dot{\theta}_m^-$), and *7)* the post-impact velocities ($\dot{x}_m^+$, $\dot{y}_m^+$, and $\dot{\theta}_m^+$).

The forces caused by the pounding occurrences affect the displacement history. Based on Table 2, the resultant forces generated by pounding, the moment produced by the resultant forces, and the change in velocities about the six pounding events are listed in Table 3. The positive and negative relations $\dot{x}_m^+ - \dot{x}_m^-$ are consistent with the resultant force in the *x*-direction. A similar situation is observed for $\dot{y}_m^+ - \dot{y}_m^-$ and the resultant force in the *y*-direction. Similarly, the relationship between the moment produced by the resultant force and $\dot{\theta}_m^+ - \dot{\theta}_m^-$ is both positive and negative. This brief comparison shows how the proposed formulation consistently relates the forces due to collisions and the corresponding change in motion.

Table 2. Key parameters of the pounding occurrences.

Pounding occurrences	1	2	3	4	5	6
Time (s)	15.045	15.240	15.885	16.445	17.290	18.145
Pounding spot	P_4	P_1 and P_2	P_1	P_3	P_1	P_3
λ_{N1} (kN)	0	7058	84820	0	82920	0
λ_{N2} (kN)	0	33332	0	0	0	0
λ_{N3} (kN)	0	0	0	52714	0	33603
λ_{N4} (kN)	91443	0	0	0	0	0
λ_{T1} (kN)	0	-2117	-25446	0	-24876	0
λ_{T2} (kN)	0	-10000	0	0	0	0
λ_{T3} (kN)	0	0	0	-1156	0	-10081
λ_{T4} (kN)	-25985	0	0	0	0	0
x_m (mm)	35.8	-59.9	-9.3	11.6	-19.3	34.6
y_m (mm)	-62.5	-17.2	-70.6	13.6	-18.1	-19.0
θ_m (rad)	-0.000339	0.0000103	-0.00123	0.00406	-0.00250	0.00149
g_{N1} (mm)	55	0	0	135	0	102
g_{N2} (mm)	58	0	9	103	19	90
g_{N3} (mm)	3	103	50	0	103	0
g_{N4} (mm)	0	103	41	31	84	11
$\dot{x}_m^-$ (mm/s)	237.4	-428.3	-517.1	-26.7	-217.8	143.5
$\dot{y}_m^-$ (mm/s)	-266.2	445.2	28.0	-602.4	-266.8	37.1
$\dot{\theta}_m^-$ (rad/s)	-0.00164	0.000474	-0.00233	0.00779	-0.00483	0.00371
$\dot{x}_m^+$ (mm/s)	-255.3	-213.1	-65.1	-362.2	224.1	-35.6
$\dot{y}_m^+$ (mm/s)	-93.4	517.4	179.6	-413.7	-118.5	97.1
$\dot{\theta}_m^+$ (rad/s)	0.00163	-0.000237	0.0117	-0.00616	0.00426	0.0000445

Table 3. Verification of motion solutions by the resultant force produced by pounding and the changes of pre- and post-impact velocities.

Pounding Occurrences	λ_{Rx} (kN)	$\dot{x}_m^+ - \dot{x}_m^-$ (mm/s)	λ_{Ry} (kN)	$\dot{y}_m^+ - \dot{y}_m^-$ (mm/s)	M_R (kNm)	$\dot{\theta}_m^+ - \dot{\theta}_m^-$ (rad/s)
1	-66197	-493	68225	173	173062	0.00328
2	23866	215	25326	72	-76805	-0.00071
3	60731	452	64446	152	516410	0.00937
4	-45072	-335	27358	189	-730520	-0.01394
5	59371	442	63002	148	484532	0.00909
6	-24060	-179	25532	60	-191634	-0.00371

Note: λ_{Rx} and λ_{Ry} denote the components of the resultant force in the *x*- and *y*-directions, respectively. M_R denotes the moment produced by the resultant force.

3.6 Verification of the results

The computational procedure can be verified according to the following three considerations:

1. If $g_{Ni} \geq 0$ and $\Lambda_{Ni} = 0$, there is no contact between point P_i and the adjacent abutment. When $\Lambda_{Ni} \geq 0$ and $g_{Ni} = 0$, the curved beam and abutment come into contact. In math expression, Λ_{Ni} and g_{Ni} should meet the LCP relationship during the time history. It can be seen in Fig. 11 that Λ_{Ni} and g_{Ni} maintain linear complementarity at all times.
2. According to Eq. (10), the values of $g_{N1} - g_{N2}$ and $g_{N4} - g_{N3}$ should be consistent during the time history. The time history of $g_{N1} - g_{N2}$ and $g_{N4} - g_{N3}$ are drawn as shown in Fig. 13. The adequacy of the computational procedure is demonstrated by the perfect congruence of the two time histories.

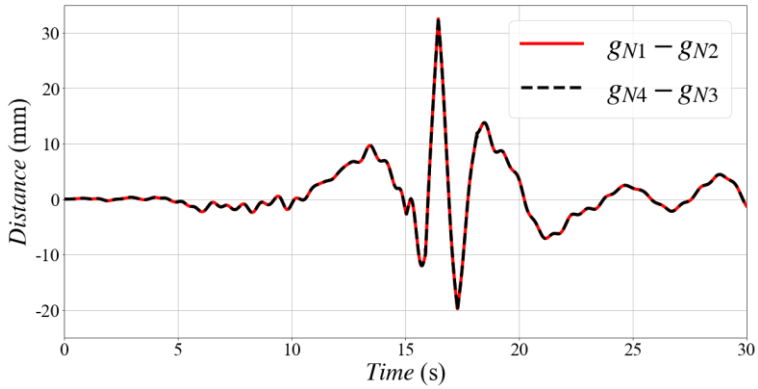

Fig. 13. Time histories of $g_{N1} - g_{N2}$ and $g_{N4} - g_{N3}$.

3. The momentum theorem should be satisfied at the moment of the pounding event, that is, the change in momentum of the curved beam should equal the impulse of the force applied to it during the pounding process at both its beginning and its end. The change in momentum and the impulse of the force during every pounding event are shown in Fig. 14, and the momentum theorem is satisfied.

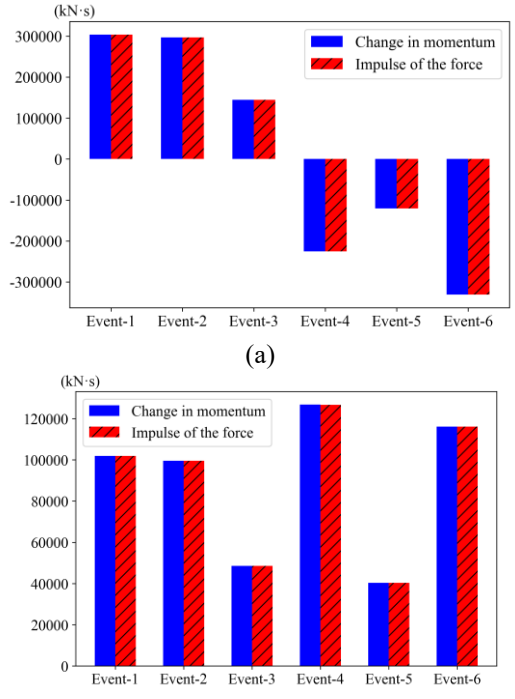

Fig. 14. The change in momentum and the impulse of the force during every pounding occurrences in the (a) *x*-; and (b) *y*-direction.

4. Conclusions

This study introduces a new method to solve the problem of the dynamic response and contact interactions of curved beam bridges modelled as rigid bodies under seismic ground motions and end-pounding effects. The method uses a non-smooth formulation to create dynamic equations of motion that account for pounding effects based on a Lagrange multipliers approach. The new formulation is presented, programmed, exemplified, and validated. The following conclusions can be drawn:

1. The seismic response of curved beam bridges can be analyzed by the proposed non-smooth formulation accounting for pounding effects based on a Lagrange multipliers approach. The dynamic equation of the curved bridge can be represented by a lumped mass and stiffness matrix. The pounding scenarios can be analyzed by considering Jacobian matrices of velocity with respect to the DOFs at some spots on the beam ends where pounding is expected. The unilateral constraints are transformed into a linear complementarity problem (LCP) formulation that relates to velocity and impulse in both normal and transverse directions. The dynamic equations of the pounding system of curved beam bridges are formulated by adding the products of impact and friction forces and their corresponding Jacobian matrices as Lagrange multipliers. Non-smooth contact differential equations are developed by appending the LCP formulation related to the velocities and impulses in the normal and transverse directions.
2. The algorithm for solving the differential equations in LCP is implemented in Matlab to identify the collision and motion states by accessing a stepwise acceleration time history.
3. To assess the effectiveness and suitability of the proposed method, a case study curved beam bridge consisting of two spans, an intermediate pier, and two adjacent abutments is subjected to a single ground motion.
4. The seismic response of the case study bridge obtained by the proposed procedure and neglecting the pounding effects is compared with the results of an 'equivalent' finite element (FE) model developed in OpenSees. The comparison shows a good match of the results.
5. The seismic response of the case study bridge is evaluated by the proposed procedure, including the pounding effects. The displacements and rotations time histories, including the end-pounding occurrences, are fully identified by the analysis. The results show the ability of the proposed procedure to capture the interrelation of the different quantities involved in the problem. For example, it can be observed that the change in velocity at the centroid of the curved beam in the x- and y-directions depends on the resultant of the normal pounding force and transverse friction force. Similarly, the change in the rotational speed of the curved beam is determined by the resultant moment created by the normal pounding force and transverse friction force.
6. Given the transient nature of the collision events, providing direct evidence for tracking the time and motion process is difficult and rarely found in the existing literature. Three verification approaches are proposed, relying on checks about the consistency in the LCP relationship, the geometric relationship, and the impulse-momentum theorem.
7. The present study neglects the influence of soil-structure interaction effects. However, in soft soils this could significantly affect the seismic response and pounding effects of the curved bridge deck and will be part of the future work in this direction. Furthermore, the effect of the different characteristics of ground motions on the pounding response of curved bridge by using non-smooth method is also a challenging issue for the researchers.

Acknowledgements

This study was supported by the National Key R&D Program of China (No. 2019YFE0119800).

References

[1] Liu Z. Reconnaissance and preliminary observations of bridge damage in the great Wenchuan earthquake, China. Structural engineering international 2009; 19(3): 277-282. doi: 10.2749/101686609788957883

[2] Williams D, Godden W. Seismic response of long curved bridge structures: experimental model studies. Earthquake Engineering & Structural Dynamics 1979; vol. 7, no. 2, pp. 107-128. doi: 10.1002/eqe.4290070202

[3] Housner GW, Thiel Jr CC. The continuing challenge: report on the performance of state bridges in the Northridge earthquake. Earthquake spectra 1995; 11(4): 607-636. doi: 10.1193/1.1585829

[4] Kosa K, Tazaki K, Yamaguchi E. Mechanism of damage to Shiwei Bridge caused by 1999 Chi-Chi earthquake. Structural Engineering/Earthquake Engineering 2002; 19(2): 221-226. doi: 10.2208/jsceseee.19.221s

[5] Miari M, Choong KK, Jankowski R. Seismic pounding between bridge segments: a state-of-the-art review. Archives of Computational Methods in Engineering 2021; 28(2): 495-504. doi: 10.1007/s11831-019-09389-x

[6] Anagnostopoulos SA. Pounding of buildings in series during earthquakes. Earthquake engineering &

structural dynamics 1988; 16(3): 443-456. doi: 10.1002/eqe.4290160311
[7] Anagnostopoulos SA. Equivalent viscous damping for modeling inelastic impacts in earthquake pounding problems. Earthquake engineering & structural dynamics 2004; 33(8): 897-902. doi: 10.1002/eqe.377
[8] Davis RO. Pounding of buildings modelled by an impact oscillator. Earthquake engineering & structural dynamics 1992; 21(3): 253-274. doi: 10.1002/eqe.4290210305
[9] Muthukumar S, DesRoches R. A Hertz contact model with non-linear damping for pounding simulation. Earthquake engineering & structural dynamics 2006; 35(7): 811-828. doi: 10.1002/eqe.557
[10] Jankowski R. Non-linear viscoelastic modelling of earthquake-induced structural pounding. Earthquake engineering & structural dynamics 2005; 34(6): 595-611. doi: 10.1002/eqe.434
[11] Jankowski R. Analytical expression between the impact damping ratio and the coefficient of restitution in the non-linear viscoelastic model of structural pounding. Earthquake engineering & structural dynamics 2006; 35(4): 517-524. doi: 10.1002/eqe.537
[12] Khatami SM, Naderpour H, Razavi SMN, barros RC, Soltysik B, Jankowski R. An ANN-based approach for prediction of sufficient seismic gap between adjacent buildings prone to earthquake-induced pounding. Applied Sciences 2020; 10(10): 3591. doi:10.3390/app10103591
[13] Raheem S.E.A, Fooly M.Y.M., Shafy A.G.A.A, Abbas Y.A, Omar M, Latif M.M.S.A, Mahmoud S. Seismic pounding effects on adjacent buildings in series with different alignment configurations. Steel and Composite Structures 2018; 28(3), 289-308. doi:10.12989/SCS.2018.28.3.289
[14] FAvvata M.J. Minimum required separation gap for adjacent RC frames with potential inter-story seismic pounding. Engineering Structures 2017; 152:643-659. Doi:10.1016/j.engstruct.2017.09.025
[15] Zu L, Huang Y. Li W. Seismic damage analysis of Yematan Bridge under near-fault earthquakes. Structures 2022; 41:586-601. doi:10.1016/j.istruc.2022.05.006
[16] Shen Y, Li J, Freddi F, Igarashi A, Zhou J. Numerical investigation of transverse steel damper (TSD) seismic system for suspension bridges considering pounding between girder and towers. Soil Dynamics and earthquake Engineering 2022; 150:107203. doi: 10.1016/j.soildyn.2022.107203
[17] Huang Y, Song G, Li G. Seismic performance of continuous curved girder bridge with high pier in Maduo earthquake and characteristic analysis. Multidiscipline Modeling in Materials and Structures 2022; 18(6):941-961. doi: 10.1108/MMMS-06-2022-0114
[18] Hao H , Bi K , Chouw N , Ren W. State-of-the-art review on seismic induced pounding response of bridge structures. Journal of earthquake and tsunami 2013; 7(03):1350019-.
[19] Skrinjar L, Slavič J, Boltežar M. A review of continuous contact-force models in multibody dynamics. International Journal of Mechanical Sciences 2018; 145:171-187.
[20] Machado M, Moreira P, Flores P, Lankarani HM. Compliant contact force models in multibody dynamics: Evolution of the Hertz contact theory. Mechanism and Machine Theory 2012; 53(0): 99-121.
[21] Banerjee A, Chanda A, Das R. Historical Origin and Recent Development on Normal Directional Impact Models for Rigid Body Contact Simulation: A Critical Review. Archives of Computational Methods in Engineering 2017; 24(2):397-422. doi: 10.1007/s11831-016-9164-5
[22] Brogliato B . Nonsmooth mechanics. Models, dynamics and control. 2nd ed. 2000.
[23] Stronge W.J. Smooth dynamics of oblique impact with friction. International Journal of Impact Engineering 2013; 51: 36-49.
[24] Slavič J, Boltežar M. Simulating multibody dynamics with rough contact surfaces and run-in-wear. Nonlinear Dynamics 2006; 45(3-4): 353-365.
[25] Bearini V, Royer-Carfagni G, Tasora A. A regularized non-smooth contact dynamics approach for architectural masonry structures. Computers & Structures 2017; 187: 88-100.
[26] Fedorova M, Sivaselvan M.V. An algorithm for dynamic vehicle-track-structure interaction analysis for high-speed trains. Engineering Structures 2017; 148: 857-877.
[27] Negrut D, Serban R, Tasora A. Posing multibody dynamics with friction and contact as a differential complementarity problem. Journal of computational and Nonlinear Dynamics, 2018; 13(1): 014503.
[28] Brogliato B, Dam A, Paoli L,Ge'not F, Abadie M. Numerical simulation of fifinite dimensional multibody nonsmooth mechanical systems. Appl Mech Rev 2002; 55(2):107 – 150. doi: 10.1115/1.1454112
[29] Dimitrakopoulos EG. Analysis of a frictional oblique impact observed in skew bridges. Non-linear Dynamics 2010; 60(4): 575-595. doi: 10.1007/s11071-009-9616-7
[30] Dimitrakopoulos EG. Nonsmooth analysis of the impact between successive skew bridge-segments. Non-linear Dynamics 2013; 74(4): 911-928. doi: 10.1007/s11071-013-1012-7
[31] Shi Z, Dimitrakopoulos EG. Nonsmooth dynamics prediction of measured bridge response involving deck-abutment pounding. Earthquake Engineering & Structural Dynamics 2017; 46(9): 1431-1452. doi: 10.1002/eqe.2863
[32] Shi Z, Dimitrakopoulos E G. Comparative evaluation of two simulation approaches of deck-abutment pounding in bridges. Engineering Structures 2017; 148: 541-551. doi: 10.1016/j.engstruct.2017.06.077
[33] Banerjee A, Chanda A, Das R. Oblique frictional unilateral contacts perceived in curved bridges. Non-linear

Dynamics 2016; 85(4): 2207-2231. doi: 10.1007/s11071-016-2824-z
[34] Li W, Huang Y, Xie G. A study on the mechanism of impact between curved bridge segments using nonsmooth dynamics. Shock and Vibration 2020; 2020. doi: 10.1155/2020/5217165
[35] Banerjee A, Chanda A, Das R. Seismic analysis of a curved bridge considering deck-abutment pounding interaction: an analytical investigation on the post-impact response. Earthquake Engineering & Structural Dynamics 2017; 46(2): 267-290. doi: 10.1002/eqe.2791
[36] Cottle RW, Pang JS, Stone RE. The linear complementarity problem. Society for Industrial and Applied Mathematics 2009. doi: 10.1137/1.9780898719000.bm
[37] Pfeiffer F, Glocker C. Multibody dynamics with unilateral contacts, John Wiley & Sons, Hoboken, HJ, USA, 1996
[38] Specifications for seismic design of highway bridges, China Communications Press Co.,Ltd., Beijing, China, 2020.
[39] McKenna F, Fenves G.L, Scott M.H. Open system for earthquake engineering simulation, Pacific Earthquake Engineering Research Center, Berkeley, CA, USA, 2010